Supplementary Information (Tosca et al.)

Magnetite Authigenesis and the Warming of Early Mars

Nicholas J. Tosca, Imad A.M. Ahmed, Benjamin M. Tutolo, Alice Ashpitel, Joel A. Hurowitz

Table S1.

Model parameters simulating the dissolution of Rocknest crystalline basalt.

Mineral	*Abundance (%)*	*Specific surface area (cm^2 g^{-1})*	*Rate constant, k (mol silicate cm^{-2} sec-1)*	*n*
Forsterite	15.1	1000	2.34E-11	0.372
Fayalite	9.3	1000	2.34E-11	0.372
Wollastonite	7.3	1000	1.99E-12	0.240
Enstatite	15.6	1000	2.51E-16	0.240
Ferrosilite	8.2	1000	7.94E-15	0.240
Albite	19.1	1000	2.38E-14	0.403
Anorthite	25.4	1000	2.31E-11	0.985

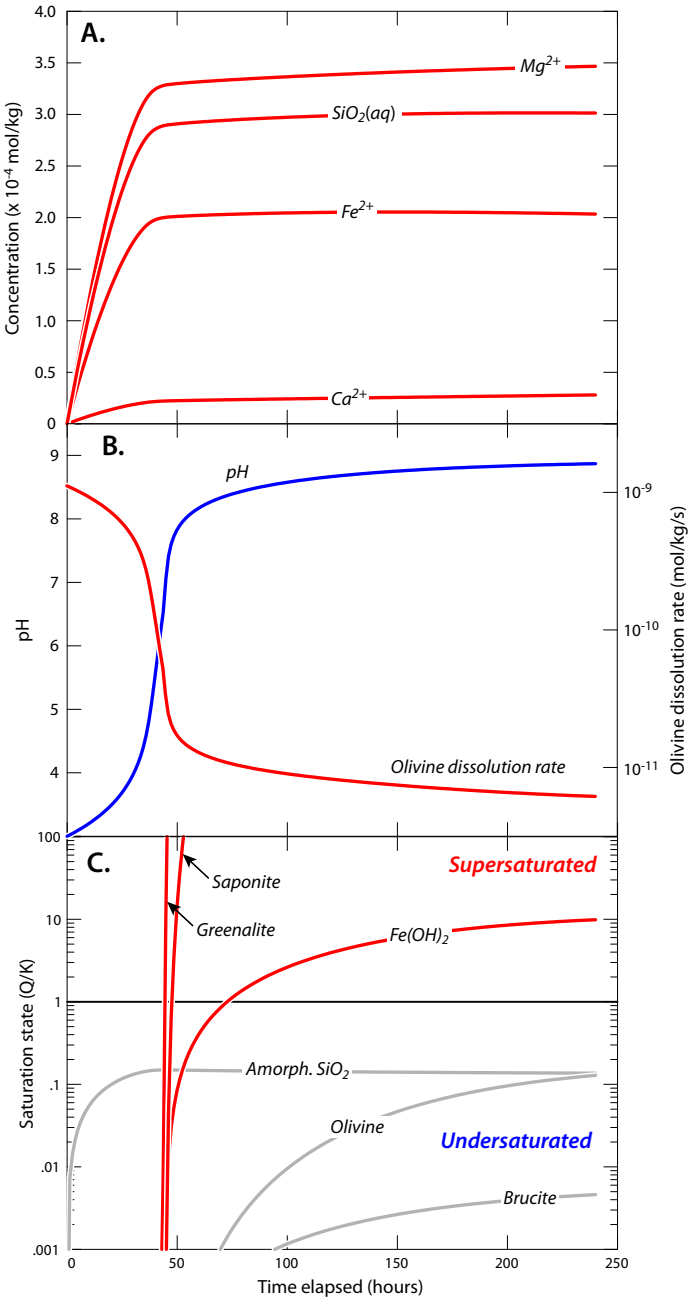

Fig. S1.

Dissolution of Rocknest basalt in weakly acidified dilute water. Concentrations of dissolved Mg^{2+}, Fe^{2+}, and $SiO_2(aq)$ **(A.)** increase rapidly, controlled mainly by olivine (Fo_{38}) dissolution. At the same time, pH increases to pH ~8.7 causing a rapid decline in silicate mineral dissolution rates **(B.)**. A number of Fe(II)-bearing precipitates reach supersaturation under these conditions **(C.)**, the identity of which is determined by the kinetics of nucleation and crystal growth. CO_2 was not considered in this calculation, as the role of CO_2 on mineral precipitation, a specific focus of this study, is discussed in the main text, and in further detail below.

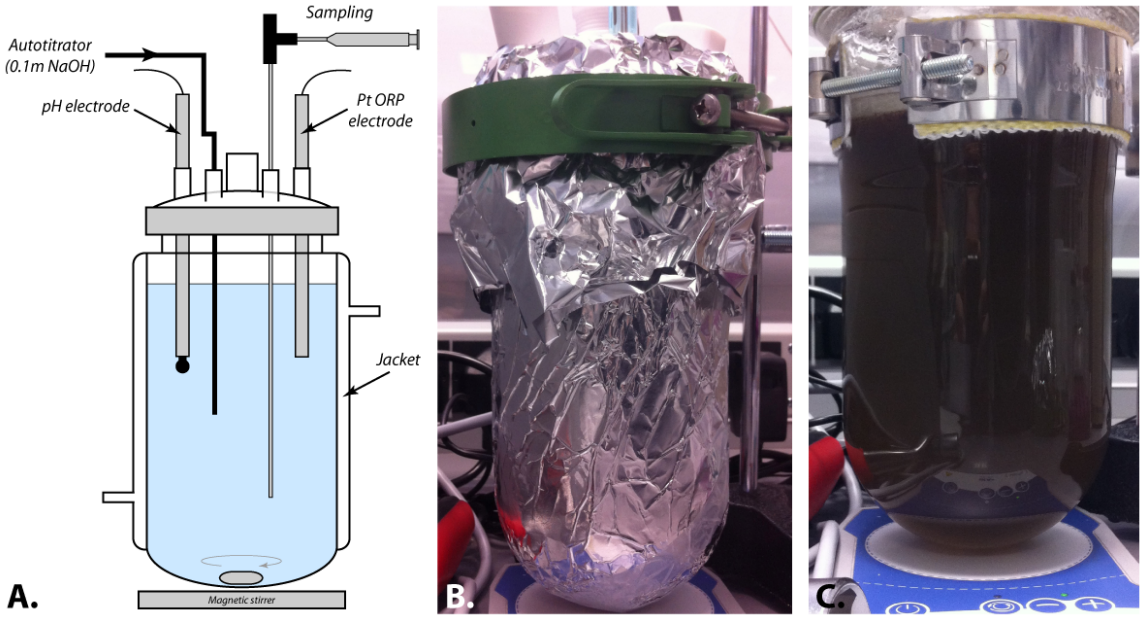

Fig. S2.

Anoxic precipitation experiments. Experimental configuration **(A.)** allows pH control by autotitration, solution/solid sampling, and in-situ monitoring of pH and ORP. All experiments were triple-wrapped with Al foil **(B.)** and conducted in the anaerobic chamber. After several days of aging $Fe(OH)_2$ and green rust precipitates at constant pH, the products are dominated by magnetite **(C.)**.

$Fe(OH)_2$ transformation to magnetite via green rust

During a typical experiment, solution chemistry indicates that Fe^{2+} is depleted rapidly in preference to both Mg^{2+} and $SiO_2(aq)$ (**Figure S3 and Figure S4**). The drawdown of Fe^{2+} corresponds to a rapid drop in the ORP of the system below the thermodynamic stability of $H_2O(l)$. Chemical analyses indicate that increasing pH resulted in supersaturation and precipitation of $Fe(OH)_2$, consistent with analyses performed on solids extracted from the experiments (**Figure 1** in the manuscript). Consistent with our previous work, the kinetics of $Fe(OH)_2$ precipitation under these conditions are typically more rapid than the nucleation of pure Fe(II)-silicates, which is often characterized by long induction periods[24].

$Fe(OH)_2$ was isolated and stabilized from selected experiments and analyzed by high-resolution TEM (data not shown) and powder X-ray diffraction. The TEM results (not shown) indicate that freshly precipitated $Fe(OH)_2$ appears as rounded, hydrous spherical particles, consistent with energetic predictions of adsorption or intercalation of H_2O into the structure[72]. In addition, Rietveld refinement conducted on powder X-ray diffraction analyses confirms a similar structure for $Fe(OH)_2$ to that reported by Parise et al.[71] (**Figure S5 and Table S2**).

The conversion of $Fe(OH)_2$ to magnetite under anoxic conditions (**Figure S2**) has been reported by a number of authors[73-79]. However, the role of intermediates such as green rust, as observed in our experiments, is unclear from early studies. For example, Schrauzer & Guth[78] synthesized suspensions of $Fe(OH)_2$ and reported the formation of magnetite and $H_2(g)$ through ageing under anoxic conditions at room temperature. These authors also observed that the conversion from $Fe(OH)_2$ to magnetite, and associated H_2 production, was accelerated by exposure to UV light and through the addition of Ni^{2+}. Similarly, Sugimoto & Matijevic[79] reported that suspensions of $Fe(OH)_2$ "gel" rapidly transformed to magnetite upon ageing under anoxic conditions at higher temperatures.

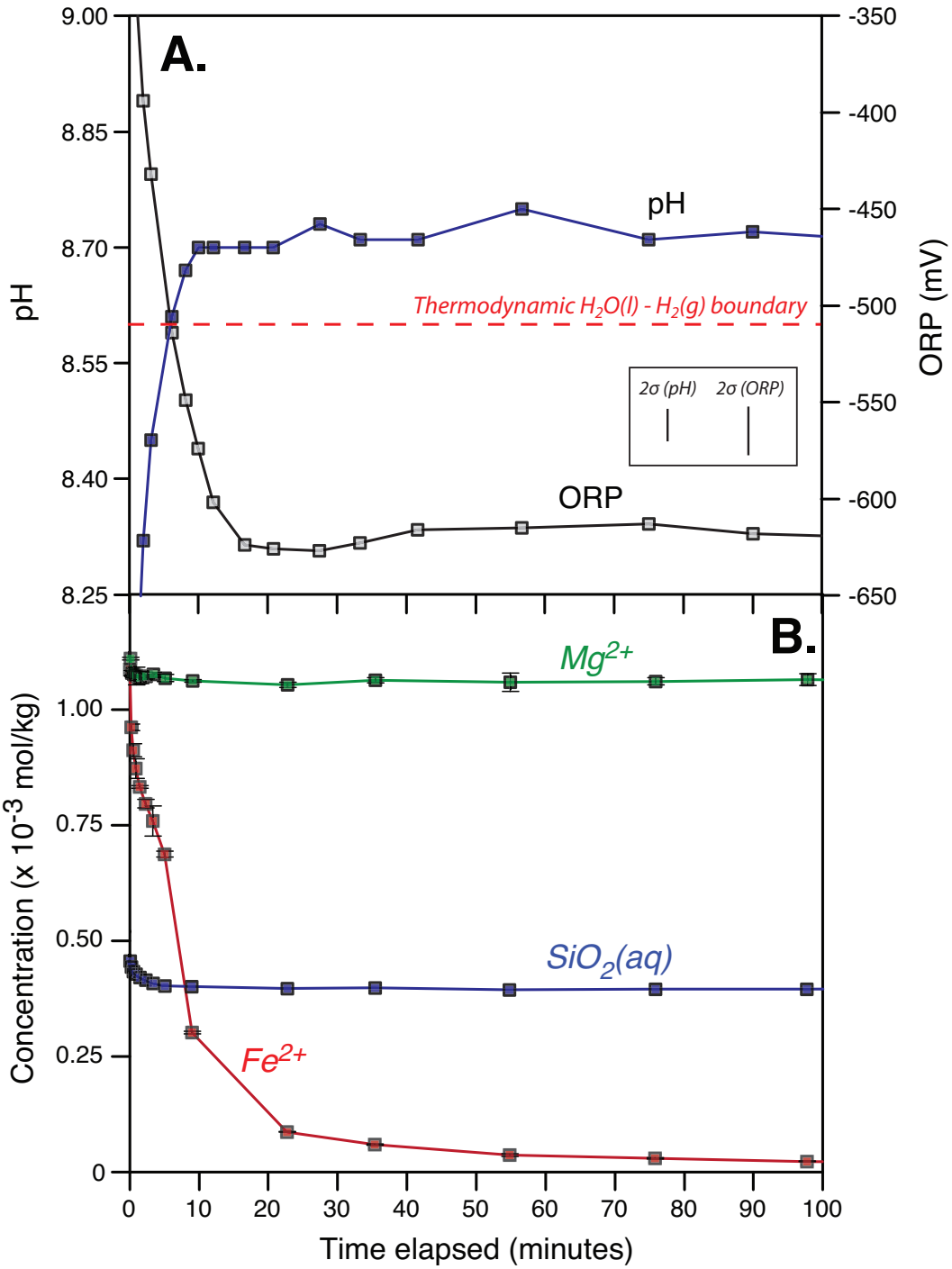

Fig. S3.

Solution chemistry during anoxic precipitation experiments. As the pH increases in anoxic Fe^{2+}, Mg^{2+} and $SiO_2(aq)$ solutions, ORP values decrease below the thermodynamic stability of $H_2O(l)$ **(A.)**. At the same time, Fe^{2+} is rapidly scavenged from solution in preference to other chemical components **(B.)**, reflecting the initial precipitation of $Fe(OH)_2$ (Figure 1 of the main text).

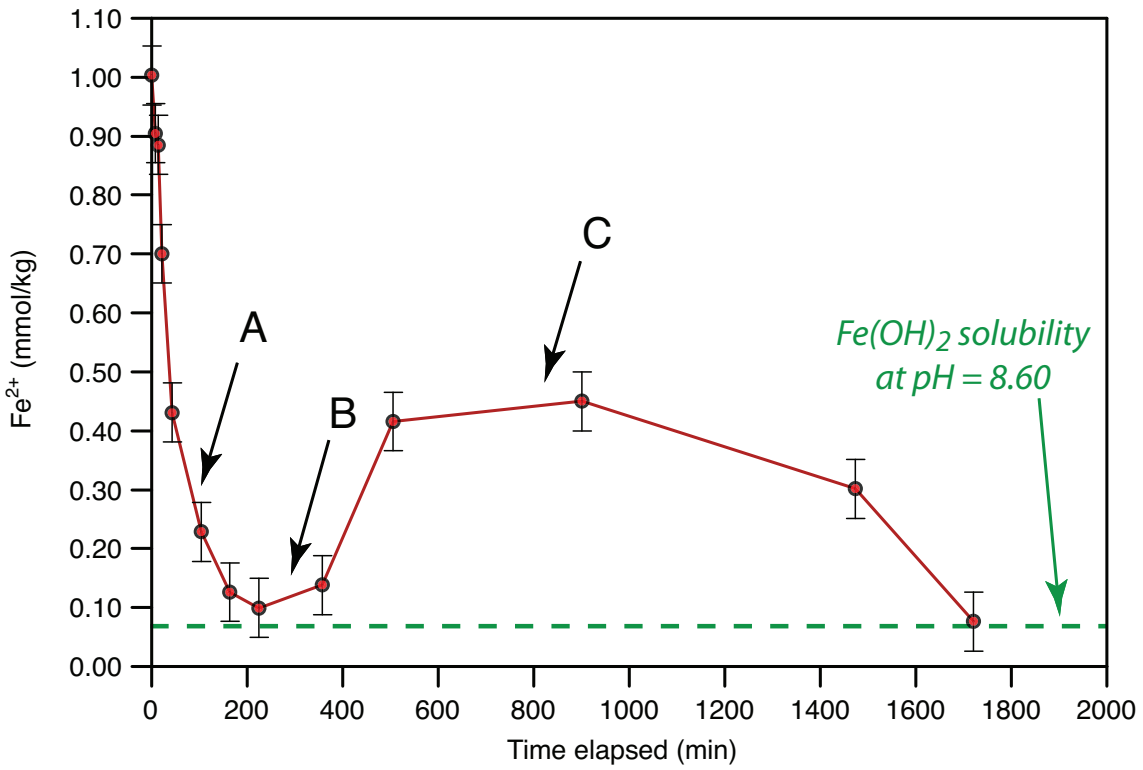

Fig. S4.

Long-term behavior of Fe^{2+} during anoxic precipitation experiment. Fe^{2+} concentrations were determined in the anaerobic chamber via UV/vis spectrophotometry (using the 1,10-phenanthroline method) during the experiment. Interval A corresponds to $Fe(OH)_2$ nucleation and transformation to green rust, as determined by *ex-situ* powder X-ray diffraction. Interval B denotes the onset of green rust transformation to magnetite via dissolution-reprecipitation, which releases Fe^{2+} into solution at levels approximately coincident with predicted stoichiometry (interval C). Finally, excess Fe^{2+} is gradually consumed through these reactions over longer intervals (greater than ~1800 minutes). At various points Fe^{2+} concentration is controlled by $Fe(OH)_2$ solubility (A, B, and at experiment termination). Experiment pH was fixed at 8.60 and initial Fe^{2+}, Mg, and $SiO_2(aq)$ were equal to 1 mmol/kg (Mg^{2+} and $SiO_2(aq)$ were invariant and are not shown).

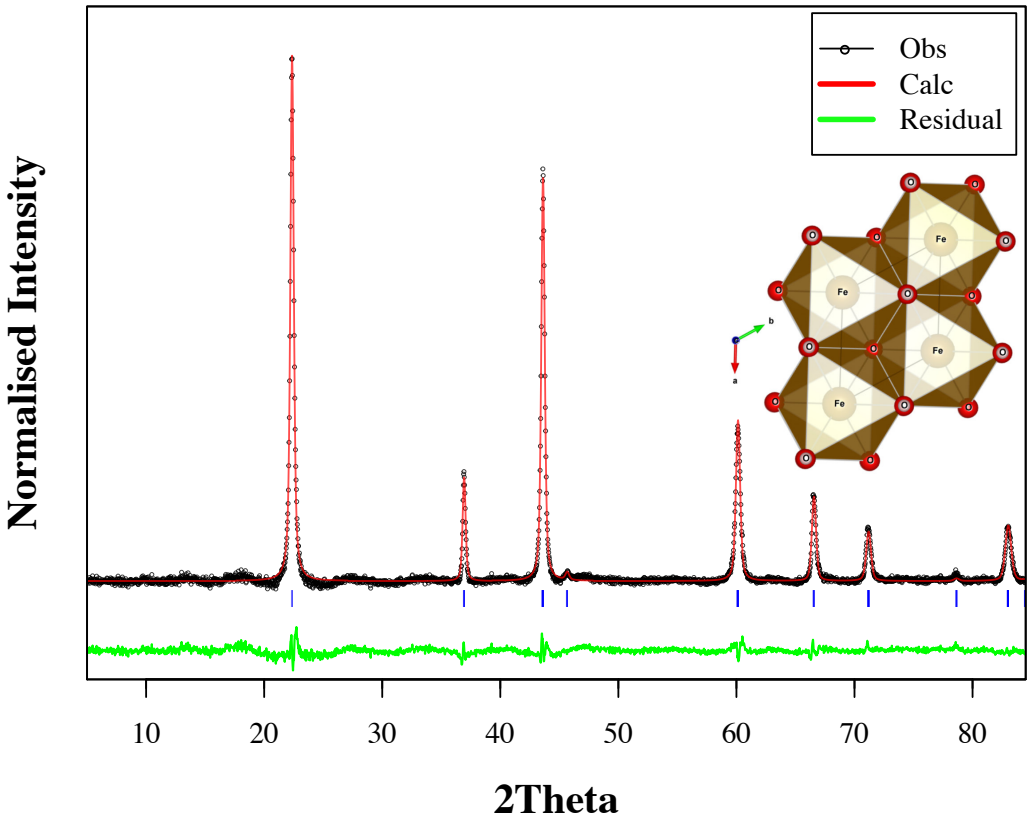

Fig. S5.

Rietveld refinement of experimental powder X-ray diffraction pattern for $Fe(OH)_2$. Structural model is shown in inset.

Table S2.

Lattice and structural parameters for $Fe(OH)_2$. Data are derived from Rietveld refinement of powder XRD patterns of experimental precipitates.

Space group	P-3m1
Unit cell volume (Å^3)	42.422896

a	b	c	α	β	γ
3.25997	3.25997	4.60938	90	90	120

	x	y	z	Occ.	U	Site	Sym.
Fe	0.00000	0.00000	0.00000	1.000	0.037	1a	-3m
O	0.33333	0.66667	0.20905	1.000	0.004	2d	3m
H	0.33333	0.66667	0.43527	1.000	0.263	2d	3m

O-H	0.96189(3) Å
Fe-O	2.11306(3) Å
Fe-Fe	3.25997(3) Å
Fe-H	2.69036(4) Å

An important difference between our results and previous studies of $Fe(OH)_2$ reactivity is that our observations indicate that as $Fe(OH)_2$ ages under anoxic conditions, green rust is formed as an intermediate phase which then converts to magnetite. This is, in fact, compatible with data presented in previous reports. Green rust and the role of solution anion composition in its formation was not widely appreciated until relatively recently[80]. Indeed, Schrauzer & Guth[78] report "greenish blue" suspensions produced upon the anoxic ageing of $Fe(OH)_2$ to magnetite, which, because fresh $Fe(OH)_2$ is white, indicates that green rust was formed as an intermediate. By considering Schrauzer & Guth's[78] experimental conditions, Wander & Schoonen[81] subsequently showed that the production of borate-containing green rust was thermodynamically favored under these conditions.

The anoxic transformation of $Fe(OH)_2$ to green rust is also supported by structural considerations. The shuttling of electrons from $Fe(OH)_2$ to H_2O eventually generates an octahedral layer composed of Fe(II) and Fe(III)[82]. The charge imbalance imparts a net positive charge to the Fe-octahedral layers, and the intercalation of anions from solution will satisfy this charge, thereby producing green rust-type compounds[80,82-85].

Consistent with these expectations, the identity of the green rust phase is determined in part by the anion content of the solution, which in our experiments is composed dominantly of SO_4, with minor Cl, and variable CO_3 (a function of pH and P_{CO2}). However, structural constraints during $Fe(OH)_2$ transformation play an important role in the identify of the green rust phase. Despite the SO_4-dominated composition of the solutions used in our experiments, we observe the initial formation of green rust-Cl, though green rust-SO_4 is also observed with time. Consistent with previous studies of the structure and formation of green rusts, the accumulation of positive charge during self-oxidation of $Fe(OH)_2$, and the resulting separation of Fe(II)-hydroxide sheets, favors the intercalation of relatively compact Cl and CO_3 ions (with basal spacings of 8.0 and 7.5 Å, respectively) over larger ions such as SO_4 (~11.1 Å), at least upon initial oxidation[85]. Thus, in the presence of sufficient CO_3^{2-}, Cl-CO_3 ion exchange leads to the dominance of CO_3-green rust, though HCO_3^- incorporation may also play a role.

As discussed in the manuscript, the conversion of $Fe(OH)_2$ to green rust demands that electrons are transferred from the structure to satisfy electron balance. Our data indicate that the electron acceptor is H_2O, which is responsible for producing $H_2(g)$. These data additionally provide unambiguous and quantitative evidence that the role of O_2 in our system is negligible. The steps taken to maintain strictly anoxic experimental conditions are described in the section entitled "Experimental Methods". However, even if we assume a maximum O_2 concentration in the anaerobic chamber of 1 ppm, a simple calculation demonstrates that the role of oxidation by O_2 is negligible in this system:

Figure 1 in the manuscript (and **Figures S3, S4 and Table S2**) shows that ~1 mmol of Fe^{2+} is rapidly precipitated as $Fe(OH)_2$. **Figure 1** also documents that, in less than 20 minutes, a significant proportion of this $Fe(OH)_2$ is transformed to green rust (~10 % of the solid by XRD, or ~0.1 mmol).

An anaerobic chamber atmospheric O_2 concentration of 1ppm translates to a dissolved $O_2(aq)$ concentration of 1.3×10^{-9} mol/L (through Henry's Law), consistent with our indigo carmine blue analysis of $O_2(aq)$ before the reaction was started (discussed above).

Therefore, if the transformation of $Fe(OH)_2$ to green rust occurred by oxidation from O_2, an $O_2(aq)$ concentration of more than 20,000 times the actual measured value would be required (note that the reaction vessel is also sealed before the experiment is started). Thus, O_2, even if present in trace amounts, cannot explain our chemical and mineralogical observations. Finally, oxidation by O_2 is not a reasonable explanation for non-stoichiometric values for H_2 production. This is because aqueous H_2 concentrations in our experiments are on the order of 40,000 times the maximum amount of $O_2(aq)$ that could be present in the system. This is further supported by abundant evidence for mineralogical products dominated by ferrous iron when other experimental conditions are examined (i.e., $FeCO_3$ XRD analyses shown below).

H_2 production through the ageing of $Fe(OH)_2$ has been observed in several studies[74,78,86], and our results are quantitatively consistent with these. Two pieces of evidence support H_2 production through $Fe(OH)_2$ conversion to green rust in our experiments. First, as discussed above, we duplicated one experiment in the anaerobic chamber purged with pure Ar gas in order to positively identify $H_2(g)$ produced during the initial stages of the experiment. H_2 gas analysis of three aqueous samples taken between 10 and 100 minutes of reaction yielded dissolved H_2 concentrations of 39 +/- 3 μmol/kg H_2. Given that approximately 1 mmol/kg $Fe(OH)_2$ was precipitated and converted to green rust in this experiment, these values translate to 39 +/- 3 μmol H_2 per mmol $Fe(OH)_2$. This quantity is less than the stoichiometry of H_2 production on the basis of the following reaction:

$$4Fe(OH)_2 + Cl^- + H^+ \rightarrow Fe_3^{II}Fe^{III}(OH)_8Cl + \frac{1}{2}H_{2(g)}$$

which demands that total conversion of ~1 mmol $Fe(OH)_2$ should produce 125 μmol H_2. We suggest that this discrepancy results from H_2 degassing during the experiments (the solutions were vigorously stirred), or that this value does not reflect the total quantity of H_2 produced because the reaction had not proceeded to completion when samples were taken. Nevertheless, our results are in approximate agreement with values reported by Schrauzer and Guth[78] who note that H_2 production through the aging of $Fe(OH)_2$ gels reaches maximum yields at pH values of approximately 8.6 corresponding to ~160 μmol H_2 per mmol $Fe(OH)_2$.

A second line of evidence supporting H_2 production through $Fe(OH)_2$ conversion to green rust is the ORP response of the aqueous system. As discussed in the main text, in the absence of other reducing compounds added or detected in our system, H_2 is the principal contributor to the transiently low ORP values during the initial stage of the experiments, broadly reflecting the timing and intensity of H_2 production, as corroborated by solid phase analyses and H_2 analyses. The ORP trends are consistent with numerous studies of $H_2(g)$-containing systems in the laboratory and natural environments where $H_2(g)$ exerts dominant control on electrode potentials, producing in some cases, potentials outside the predicted thermodynamic stability of water[87-90]. In addition, the ORP measurements recorded as part of our study, reflecting the $Fe(OH)_2$ to green rust transformation, are in quantitative agreement with a number of potentiometric studies of this system using identical methods[83-85,91,92]. However, derivation of the amount of H_2 produced during the initial stages of the experiments from ORP alone is not possible because of complicating factors such as the timescale of electrode responses relative to the kinetics of H_2 generation, absorption of H_2 by the Pt electrode and the assumption that electrochemical equilibrium between H_2 and the Pt electrode is established at the time of measurement[89,90].

Once green rust forms from the anoxic transformation of $Fe(OH)_2$, it rapidly recrystallizes to magnetite under anoxic conditions. This is mainly because newly formed green rust is exposed to a solution pH at which it is metastable (**Figure 1** in the manuscript, and **Figure S3 and Figure S4**). It is well known from environmental geochemistry literature that green rust is metastable with respect to magnetite under anoxic conditions in the pH range of 7-9[80,93-95]. This transformation has been observed in-situ through synchrotron-based techniques[95], and through the anoxic titration of Fe-CO_2-SO_4 systems[94]. It is important to note that several experimental studies investigating the conversion of green rust to magnetite show that this transformation proceeds by dissolution-reprecipitation (rather than by oxidation and H_2 production). This process can be expressed as:

$$\underset{\text{Green rust}}{2Fe^{II}_3Fe^{III}(OH)_8Cl} + 8H^+ \rightarrow \underset{\text{Magnetite}}{Fe^{II}Fe^{III}_2O_4} + 12H_2O + 5Fe^{2+} + 2Cl^-$$

This reaction, as written, predicts that the conversion of green rust to magnetite involves the release of ferrous iron as Fe^{2+} as shown in **Figure S4** (and therefore no change in redox state or H_2 production). Consistent with this, several studies have documented that if green rust is perturbed into a pH range outside of its stability window, dissolution-reprecipitation will take place and magnetite will be formed. For example, this has been documented in detail by Hansen (2001)[80], Ruby et al. (2006)[93], and Guilbaud et al. (2013)[94]. The latter study documented that the onset of dissolution-reprecipitation and magnetite formation occurs at pH ~8 and higher for green rust sulphate and green rust carbonate. Furthermore, Ruby et al. (2006)[93] have documented the same process, and have found that, in addition to magnetite formation, at very high pH the Fe^{2+} produced from the process is re-precipitated as $Fe(OH)_2$ and/or $FeCO_3$. However, Guilbaud et al. (2013)[94], working at lower pH levels (~8 and higher), only identified magnetite, and did not identify any solid phase Fe^{II} products, indicating that the pH of green rust to magnetite transformation is important in controlling the fate of Fe^{2+} released from this reaction. Together, these studies are consistent with our results in that the main phase of H_2 generation derives from $Fe(OH)_2$ transformation to green rust, and little to no H_2 generation is associated with the dissolution/reprecipitation of green rust to magnetite.

The pathway we describe for magnetite precipitation is also consistent with crystal chemical constraints derived from Sheepbed magnetite from the Chemin instrument[3]. Rietveld refinement of the magnetite produced in our experiments yields lattice parameters corresponding to ideal, stoichiometric magnetite (**Figure S6 and Table S3**). Importantly, however, the magnetite produced through this anoxic pathway is finely crystalline (10's to 100's of nanometers in size). Murad & Schwertmann[96] observed that magnetite of this crystal size is highly susceptible to oxidation in O_2-containing atmospheres. They observed that after only 8 years exposure, finely crystalline magnetite oxidized extensively and led to a contracted unit cell similar to that observed for Sheepbed magnetite samples[3]. Similarly, Tang et al.[97] found that oxidation of nano-crystalline magnetite with a domain size of ~9 nm proceeded to completion in dilute, oxidized water after only 3 months. Thus, exposure to even minor amounts of atmospheric oxygen for ~3.5 billion years after formation would be expected to result in significant oxidation. This possibility was suggested by Vaniman et al.[3].

Table S3.

Lattice and structural parameters for magnetite. Data are derived from Rietveld refinement of powder XRD patterns of experimental precipitates.

Space group	Fd-3m
Unit cell volume (Å^3)	589.521842

a	b	c	α	β	γ
8.38494	8.38494	8.38494	90	90	90

	x	y	z	Occ.	U	Site	Sym.
Fe(III)	0.12500	0.12500	0.125000	1.000	0.058	8a	-43m
Fe(II)	0.50000	0.50000	0.50000	1.000	0.101	16d	.-3m
O	0.26059	0.26059	0.26059	1.000	0.038	32e	.3m

Fe(III) - O1	1.9692(17) Å
Fe(II) - O1	2.0114(17) Å
Fe(II) - Fe(II)	2.96452(4) Å
Fe(II)-Fe(III)	3.47621(5) Å

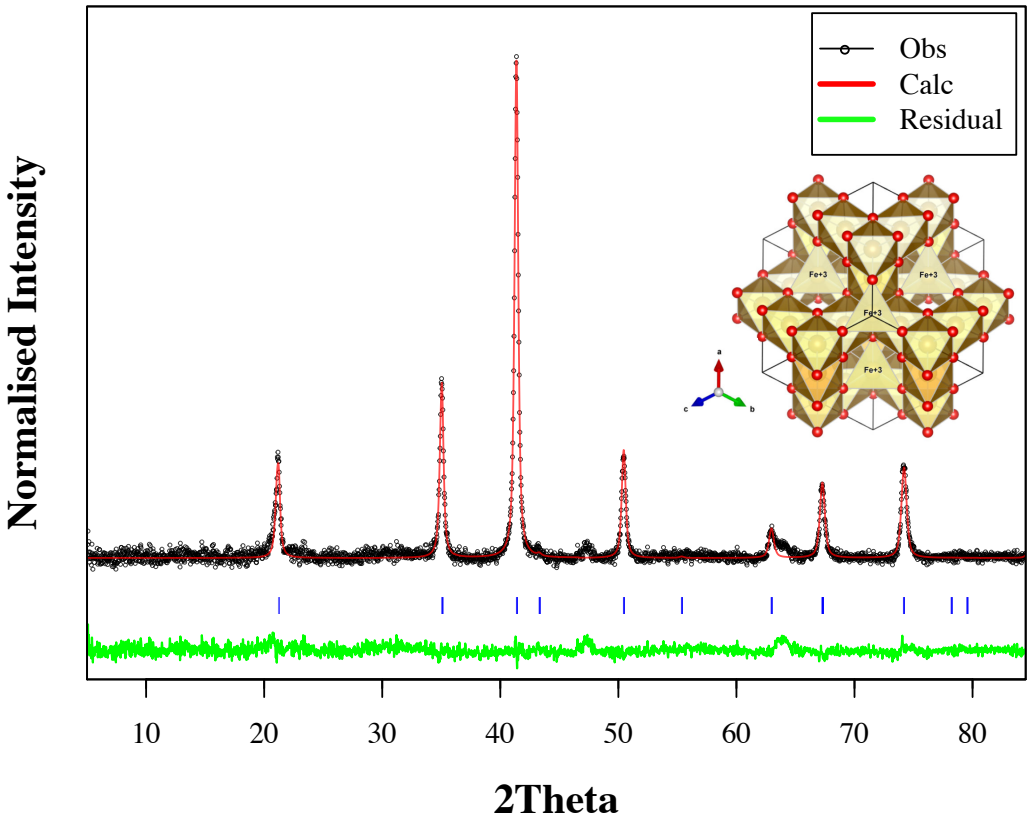

Fig. S6.

Rietveld refinement of experimental powder X-ray diffraction pattern for magnetite. Structural model is shown in inset.

Kinetics of Fe(II)-carbonate precipitation

As discussed in the manuscript, precipitation experiments in the presence of dissolved CO_2 indicate that Fe(II)-carbonate nucleation does not occur until significant supersaturation with respect to siderite is reached. The point of supersaturation required for nucleation is consistent across P_{CO2} and pH, as indicated by **Figure 2** in the manuscript. We derived this value through a best fit across all experimental conditions shown in **Figure 2**. This value, which we term the critical supersaturation, or K_{crit} (equal to $10^{-7.64}$, corresponding to the $FeCO_3$ dissolution reaction), is in good agreement with a recent study of amorphous iron carbonate (AFC) precipitation[23]. In their study, Dideriksen et al.[23] documented the precipitation and rapid (within minutes) ageing of AFC to either siderite or chukanovite, depending on pH and CO_3^{2-} ion availability. These results are consistent with our experiments which show that at high pH chukanovite dominates Fe(II)-carbonate products and at lower pH, siderite occurs (**Figure S7**).

The initial nucleation of AFC at high supersaturation offers a low energy pathway to Fe(II)-carbonate precipitation[23,26,98], analogous to amorphous $CaCO_3$ and the crystallization of $CaCO_3$ polymorphs. Sel et al.[26] argued that a direct relationship between the enthalpy of crystallization and ionic radius is a possible factor explaining why AFC is more metastable than amorphous $CaCO_3$. In fact, Sel et al.[26] note that amorphous precursors have been identified in a number of chemical synthesis studies of Fe(II)-carbonate[99-101]. Similarly, Dideriksen et al.[23] noted circumstantial evidence that AFC may have gone undetected in previous syntheses of the Fe(II)-carbonate system based on identical but distinctive morphology (also observed in our experiments).

The high supersaturation required to precipitate Fe(II)-carbonate is also consistent with experimental data and some studies of natural reducing waters on Earth where siderite is predicted, but is not observed. For example, Romanek et al.[102] reported a number of syntheses that produced siderite and Fe-bearing carbonate, but required significant supersaturation. The saturation states of each synthesis conducted by Romanek et al.[102] are consistent with K_{crit} derived from our work. Similarly, Weisli et al.[103] synthesized siderite at supersaturation levels consistent with our work, and also reported morphology consistent with AFC as discussed by Dideriksen et al.[23]. The significant supersaturation levels required for Fe(II)-carbonate precipitation and low growth rates of siderite once it nucleates from solution[104,105] both explain why numerous studies of natural anoxic waters persist at supersaturation with respect to siderite.

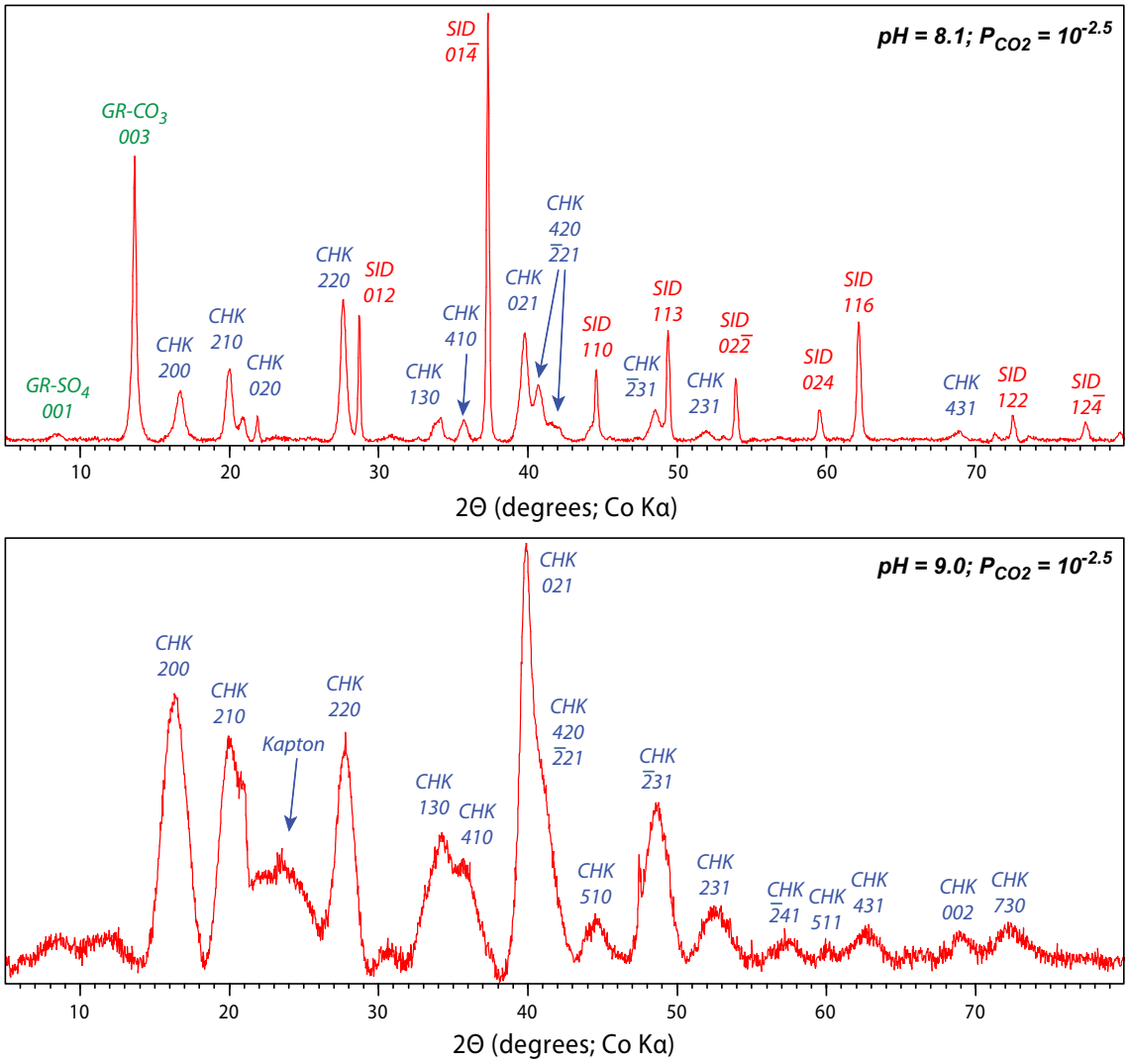

Fig. S7.

Fe(II)-carbonate precipitates. Powder X-ray diffractograms showing Fe(II)-carbonate precipitates generated at pH 8.1 (top panel) and pH 9.0 (bottom panel). GR: green rust; SID: siderite; CHK: chukanovite. Both experiments were run for a total of 16 days.

H_2 production and gas bubble generation in Gale Crater mudstones

Both solid (i.e., mineral-filled) and hollow nodules have been identified as diagenetic features in Gale Crater mudstones. For example, the Sheepbed member of the Yellowknife Bay formation contains millimeter-scale hollow nodules displaying circular rims with hollow centers[1,36]. In their evaluation of nodule formation mechanisms, Grotzinger et al.[1] and Stack et al.[36] discussed two possible origins for hollow nodules in the Sheepbed mudstone: (1) dissolution of pre-existing spherules, or (2) gas bubble formation. However, with no evidence to support the first hypothesis, both favored the second hypothesis. To evaluate whether H_2 production through magnetite formation could provide a viable mechanism for the formation of hollow nodules observed in Gale Crater mudstones, we estimated the total volume occupied by hollow nodules per cubic meter of outcrop. Outcrop observations indicate that the average diameter of hollow nodules is 0.77 mm, translating to a volume of 0.18 mm^3 (or 1.80×10^{-4} cm^3) per nodule[1,36]. In addition, imaging yields 27456 hollow nodules per m^3 of outcrop[1,36]. This translates to a total H_2 volume (represented by hollow nodules only) of approximately 2.74 cm^3 H_2 per cubic meter of outcrop.

By assuming an average outcrop density of 2.8 g/cm^3, and with H_2 obeying the ideal gas law, we can use the amount of magnetite present in the Cumberland drill hole sample and assume that the amount of H_2 produced is dictated by the stoichiometry of the overall reaction, as observed in our experiments. This equated to a 1:1 stoichiometric ratio between authigenic magnetite and H_2.

Thus, authigenic magnetite abundances for John Klein and Cumberland targets (3.3 and 4.4 wt %, respectively[3]) translate to approximately 2.8-3.7 cm^3 H_2 per cubic meter of outcrop. This estimate is in good agreement with volume estimated on the basis of hollow nodules alone, and a slightly lower estimate for the latter is consistent with H_2 residing in pore space not reflected by hollow nodules such as inter granular pore space or syneresis cracks, which have also been discussed as early diagenetic features resulting from gas production in the Sheepbed mudstone[106].

Model constraints on water chemistry in the Gale lake

Using the kinetic model of Gale Crater basalt dissolution discussed above, we examine first order controls on lake chemistry and mineral saturation state using experimentally-determined values for the nucleation of Fe(II)-carbonates from solution (using K_{crit} from Figure 2 of the main text). For the lake, we specify an open system with respect to atmospheric CO_2 and aqueous solution, so that constant solution-gas equilibration is maintained. In addition, we examine a variety of water to rock ratios (W/R = 2000 in the example shown in **Figure S8**). The disadvantage of this treatment is that the simulation is static, examining lake chemical evolution in the absence of additional sediment delivery. However, an advantage is that this treatment avoids uncertainties in sedimentation rate. As discussed in the main text, this approach assumes that at constant sedimentation rate, the mass of sediment delivered to the lake is equal to the mass of sediment for which diffusional contact with lake bottom water is severed through burial, effectively behaving as a fixed water to rock ratio system. We do not explicitly model water-rock

reactions during sediment burial, under the assumption that as sediment was accumulated, diffusive contact between pore and lake water was lost as lake bottom sediments were buried.

Our model results indicate that as fine-grained sediment interacts with lake water and dissolution proceeds, pH is rapidly increased through initial dissolution, but further increases in pH are attenuated by the dominance of CO_2 acid-base buffering under high P_{CO2} conditions (**Figure S8**). Dissolution continues over the long term, releasing all components into solution (note Mg is dominantly contained in olivine, which reaches a lower dissolution rate than other rock-forming silicates). As $SiO_2(aq)$ increases, amorphous silica solubility acts as an effective maximum on its concentration (**Figure S8**).

It is important to note that these calculations are conservative estimates of the pH status and atmospheric P_{CO2} in equilibrium with the lake. This is because additional acid sources may have contributed to lowering lake water pH, for example Fe^{2+} oxidation in surface waters[5,107] or atmospheric sulfuric acid addition as a source of SO_4. While the former acid source has been discussed extensively in the context of Gale Crater lake geochemistry, the latter is difficult to quantify, though must be consistent with bulk geochemistry, which indicates these sources were moderate[4]. Therefore, we consider the case where CO_2 represents the sole source of acid to the lake. As discussed below, lower lake water pH levels, in response to higher P_{CO2} or external acid sources, require higher proportions of groundwater infiltration to generate observed diagenetic mineralogy.

Lastly, it is important to note that clay mineral precipitation is not treated in this model (though is treated in the reactive transport model discussed below), despite the presence of clay minerals in Gale Crater mudstones. There are several reasons for this. The first is that although clay minerals have been identified in Gale Crater mudstones, the timing of their formation with respect to magnetite is uncertain[1,3,7,108]. Nevertheless, our experimental results show that when saturation is reached with respect to $Fe(OH)_2$ and/or Fe(II)-carbonates, these minerals precipitate much more rapidly than clay minerals[109]. In fact, silicate minerals have not been observed in our experiments, owing to long induction periods for nucleation and relatively slow growth rates. Thus, $Fe(OH)_2$ and Fe(II)-carbonates represent minerals which are expected to dominate incipient phases of chemical sedimentation, whereas clay minerals represent water-rock interaction over longer timescales. In addition, a thermodynamic treatment of clay mineral precipitation would actually attenuate further cation release into solution, as the solubility of clay minerals is exceedingly low[110]. Such a treatment would be inconsistent with a number of natural waters and lakes, in particular those that contain Fe (for example, Lake Matano[111]). Solubility equilibrium between water and clay is rarely, if ever, reached in natural systems for the reasons discussed above[112]. Finally, by leaving clay minerals out of long-term estimations of lake water chemical evolution, solute release can be treated as a maximum estimate as these concentrations do not reflect secondary mineral precipitation (with the exception of secondary amorphous silica). This therefore provides a maximum estimate of carbonate mineral saturation state under high CO_2 conditions for lake waters in contact with fine-grained basaltic sediment.

Constraints on basaltic aquifer water chemistry from terrestrial analogs

In addition to first order controls on lake chemistry, examination of groundwater infiltration requires constraints on the nature of basaltic groundwater itself. As discussed in the manuscript,

a number of studies report groundwater compositions for basaltic aquifers on Earth[31,113-115]. Iceland, in particular, is well studied in this regard. Arnorsson et al.[31] report chemical compositions of river, spring, and groundwaters from the Skagafjördur region in northern Iceland, dominated by fresh olivine-bearing tholeiitic basalt flows and covering a watershed of 3650 km^2. 54 groundwater compositions taken from high and low topographic areas reported in this database are plotted as a function of *in-situ* pH, temperature, total dissolved inorganic carbon, and dissolved oxygen (**Figure S9**). These data clearly show that as ground waters flowing through mafic subsurface aquifers lose atmospheric CO_2 through the precipitation of secondary carbonate minerals, buffering capacity is lost and pH plateaus to levels of ~10. Average dissolved inorganic carbon concentration of these waters is equivalent to equilibrium P_{CO2} of $10^{-5.8}$.

Our reactive transport simulations, therefore, specify solubility equilibrium with siderite and $Fe(OH)_2$ under the assumption that reaction with wall rock precipitated these minerals along the subsurface flow path. In fact, these assumptions produce water compositions identical to those displayed in **Figure S9**, reported by Arnorsson et al.[31]. Similar groundwater compositions have also been reported by Barnes and O'Neil[32] and Morill et al.[88] for ultramafic aquifers in California, by Neal & Stanger[114] for ultramafic aquifers in Oman, and by Monnin et al.[115] for ultramafic waters from New Caledonia. Interestingly, these sites are also accompanied by low temperature H_2 production, which may reflect the precipitation and ageing of $Fe(OH)_2$ at alkaline conditions along groundwater flow paths, as initially suggested by Neal & Stanger[114].

Finally, the relatively high pH reached by subsurface groundwaters percolating through basalt is dominantly a function of the acid-base surface chemistry of mafic minerals as the buffering capacity of atmospheric components is progressively lost. A surface chemistry study of forsteritic olivine by Pokrovsky and Schott[116] clearly illustrates this effect. The authors demonstrated that the pH of initially pure water reaches a steady state value at ~10 as the surface area of olivine in contact with that water increases (their Figure 11). Thus, in rock-dominated fluids at the subsurface where surface area to fluid ratios are high and flow rates are low, minerals such as olivine primarily control pH through protonation-deprotonation reactions at their surface.

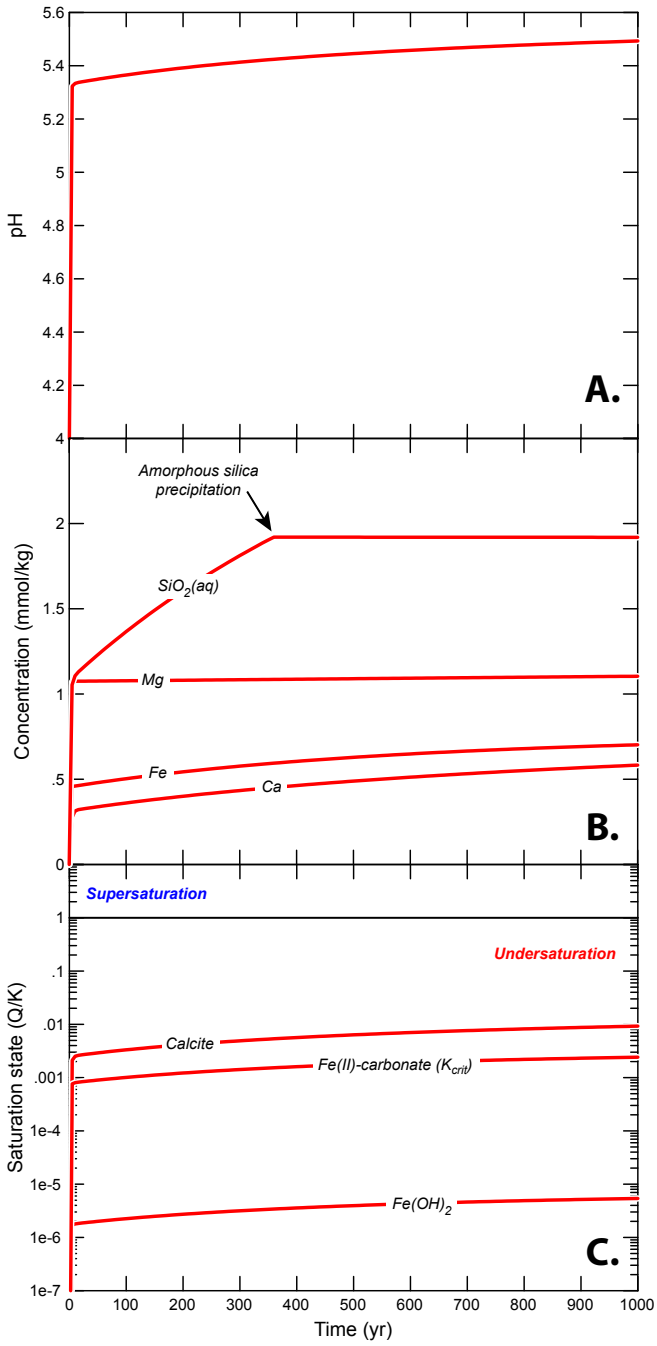

Fig. S8.

Chemical evolution of Gale Crater lake water. Using experimentally-derived data (K_{crit}) for Fe(II)-carbonates and specifying open system equilibrium with respect to a 1 bar CO_2 atmosphere, lake water, characterized by elevated total water-rock ratios, persists at relatively low pH **(A.)** without precipitating carbonate minerals or $Fe(OH)_2$ **(B., C.)**. These calculations conservatively assume no additional acid sources to the lake, which would further decrease carbonate saturation state and therefore require higher proportions of groundwater infiltration to generate observed diagenetic mineralogy.

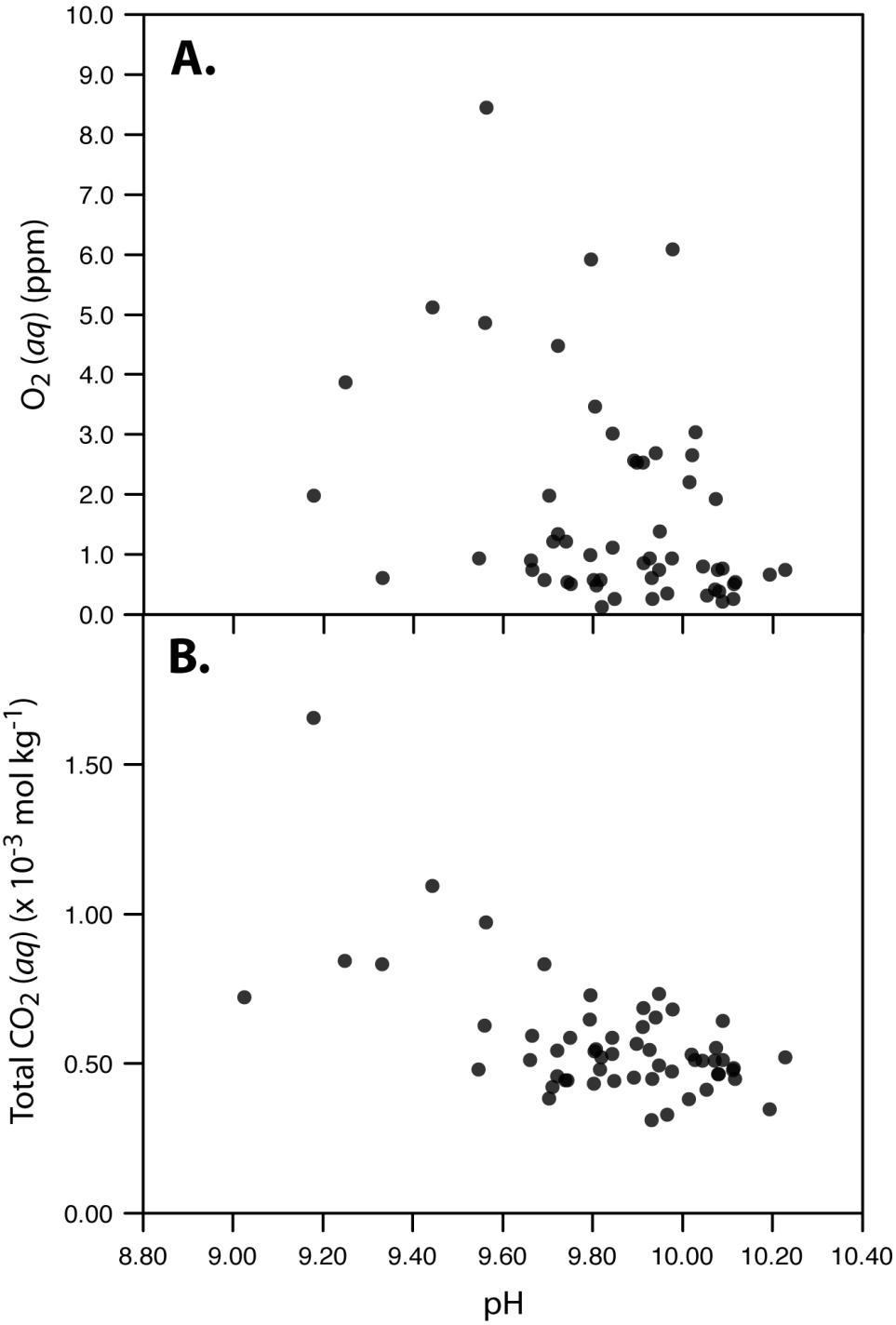

Fig. S9.

Chemistry of sub-surface waters percolating through basaltic aquifers. Data are from Arnorsson et al. (2002)[31]. As sub-surface waters react with tholeiitic olivine-bearing wall rock, O_2 **(A.)** and CO_2 **(B.)** are depleted as pH plateaus to ~10.0.

Reactive transport simulations of groundwater-lake water mixing

To examine the coupled processes of olivine dissolution, $Fe(OH)_2$ nucleation, and the transformation of $Fe(OH)_2$ to magnetite and coupled H_2 production in a geologic setting, we generated a model system for the Gale Crater sediments using the fully coupled reactive transport simulator PFLOTRAN[117]. The simulated domain consists of a 100 cm column of lake sediments with a constant porosity of 0.6 and a tortuosity of 0.5, values which are characteristic of lacustrine sediments during their most reactive phase prior to significant compaction and removal of diffusive contact with overlying lake waters[118]. The domain is in diffusive contact with pore fluids determined to be representative of basaltic groundwater at its bottom boundary, and an atmospherically-equilibrated lake water of constant composition at its upper boundary. Solute transport within the domain is diffusively controlled, assuming an average molecular diffusivity of $1x10^{-9}$ m^2/s, which is representative for low-temperature diffusivity of the relevant aqueous species[119]. Mineralogical observations of Gale Crater sediments indicate significant decreases in the modal abundance of olivine coupled to significant increases in the modal abundance of magnetite subsequent to initial sediment deposition, while other primary minerals (feldspar and pyroxene) appear to have been considerably less reactive. Thus, to avoid unnecessary complexity that comes with constraining the rates and mechanisms of reaction with these other phases, minerals other than olivine in the analyzed Gale Crater sediments **(Table S1**) were not simulated chemically. Nonetheless, their contributions to the solid volume fraction and hence porosity were explicitly considered.

Minerals in Gale Crater sediments likely to have formed after initial sediment deposition include magnetite, saponite, and amorphous silica. The critical supersaturations required to precipitate $Fe(OH)_2$ and siderite, as constrained experimentally in this study, were incorporated directly into the model. Nevertheless, simulated pore fluids never achieved the critical supersaturations required to precipitate the latter phase. Precipitation of amorphous silica was not directly simulated, as it is expected that the ultimate source for this silica would be one of the more silica-rich minerals in the sediments (i.e., plagioclase or pyroxene). Greenalite ($Fe_3Si_2O_5(OH)_4$) and chrysotile ($Mg_3Si_2O_5(OH)_4$), common byproducts of olivine-solution interactions, were incorporated into the model to serve as proxies for saponite ($Na_{0.35}Fe_3Al_{0.35}Si_{3.65}O_{10}(OH)_2$, $Na_{0.35}Mg_3Al_{0.35}Si_{3.65}O_{10}(OH)_2$,) since the model was designed to isolate the effects of olivine-solution interactions and hence did not include plagioclase, the dominant source of both Na and Al for saponite precipitation. This parameterization negligibly affects the simulation of our focus process, i.e., Fe behavior during olivine-water interaction, both because olivine has no thermodynamic stability in the presence of water at temperatures under ~ 350°C (and thus no dependence on the identity of co-existing alteration phases) and because the various Fe-bearing sheet silicates, by analogy with their magnesian counterparts, are expected to have similar apparent solubilities at low temperature[120]. The kinetics of secondary mineral precipitation were formulated within the model such that solution saturation state never significantly exceeded the experimentally-defined, critical saturation (in the case of $Fe(OH)_2$) or its thermodynamic solubility (in the case serpentine). In the simulations, Fe derived from kinetically-controlled (**Table S1**) olivine dissolution precipitates stoichiometrically as greenalite and $Fe(OH)_2$. $Fe(OH)_2$ is then transformed to magnetite through the reaction:

$$3\ Fe(OH)_2 = \text{magnetite} + 2\ H_2O + H_2(aq)\ ,$$

which we have directly incorporated into a modified version of the PFLOTRAN source code. Although our experimental results have shown that the H_2 that we actually measure is less than the stoichiometrically-predicted total above, we have no evidence to suggest that the overall H_2 produced from the reaction is less than stoichiometric.

The volume fraction of olivine and magnetite and the concentration of H_2 were monitored through the entire domain (**Figure S10**) and at the mid-point of the simulated domain (i.e,. 50 cm from each diffusive boundary) and plotted as a function of the fraction of olivine reacted (**Figure 3 & Figure S11**). Plotting the results in this way, rather than as a function of time, allows for the uncertainties associated with the well-known field-lab rate discrepancy for silicate minerals[121] to be avoided while still yielding useful results. Because the nucleation of $Fe(OH)_2$ and its conversion to magnetite are geologically rapid (as shown by the production of magnetite from $Fe(OH)_2$ in days; **Figure 1B**), the rates of these reactions are ultimately only limited by the prescribed dissolution rate of olivine, which, although geologically rapid, can be limited by a wide variety of hydrogeochemical processes[121].

Although it was not permitted to precipitate, simulated results also indicate amorphous silica supersaturation near the upper boundary of the domain where low-pH lake waters mix with high-pH groundwaters. In addition to this mechanism for amorphous silica production, amorphous silica has been observed an experimental byproduct of olivine-solution interactions at low temperature[122], a pathway which, if it were in play in Gale sediments, would allow more Fe to precipitate as $Fe(OH)_2$ and eventually magnetite. Moreover, additional Fe could have been derived from the (unsimulated) ferrosilite component of pyroxene. Lastly, although our model simulates Fe partitioning into secondary phases according to the stoichiometric reaction of olivine to Fe,Mg-serpentine, it is possible if not likely that the reaction would favor $Fe(OH)_2$ precipitation, due to the known kinetic barriers to Fe-silicate production at low temperatures[24]. For these reasons, the results plotted in **Figure 3** and **Figure S11** represent conservative estimates of the volume of magnetite precipitation and H_2 production.

Other factors, such as porosity variations due to varying sedimentation or compaction rates, could also affect our simulated results but would be unlikely to impact our overall conclusions. Porosity variations could affect our results in the following ways: 1) By increasing or decreasing the local volume of fluid, amount of olivine dissolution required to supersaturate $Fe(OH)_2$ would increase or decrease, respectively; and 2) Because sediment diffusivity ultimately depends on its porosity, higher porosities could permit low-pH lake solutions to diffuse more rapidly into the sediments and inhibit the supersaturation of $Fe(OH)_2$. In regard to both of these factors, the porosity utilized in our model (0.6), which is near the upper limit of the range of lacustrine sediment porosities, represents a conservative scenario. Moreover, in simulations run to examine the effect of lake water advection/diffusion into the sediments (i.e., an extreme downward flux of lake water of 1 cm/year), a ~10 cm "no magnetite" zone develops at the upper boundary of the domain, and in fact creates a zone akin to the lake water we use as a lake water boundary constraint. Below this zone, olivine-pore water interactions counteract this diffusive flux and yield results nearly identical to those plotted in **Figure 3 and Figure S11**. Although this latter scenario is unrealistic (the lake(s) were situated in the lowest depression for thousands of kilometers in any direction and regional hydrological models show that groundwater influx was an important component), it demonstrates the robustness of our

conclusion that magnetite production by way of a $Fe(OH)_2$ pathway could have generated a significant H_2 flux to the Martian atmosphere.

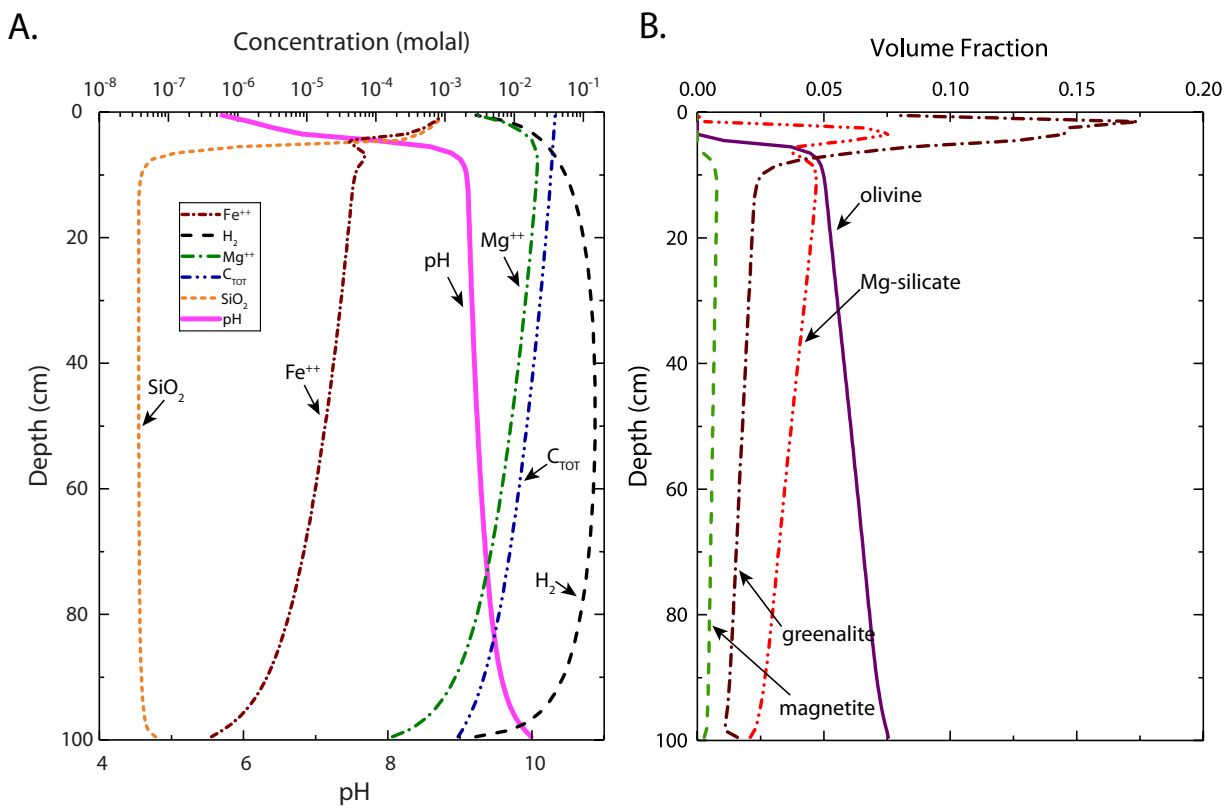

Fig. S10

Representative results of reactive transport simulations, plotted as a function of depth in the simulated domain after 10 years of simulated time, when the reaction regime has reached a quasi-steady state: **A.** Concentration of aqueous species; **B.** Volume fraction of minerals. This is a full-domain snapshot of the results plotted in Fig. 3. of the manuscript. Note that the results plotted in Fig. 3 represent the values at 50 cm depth.

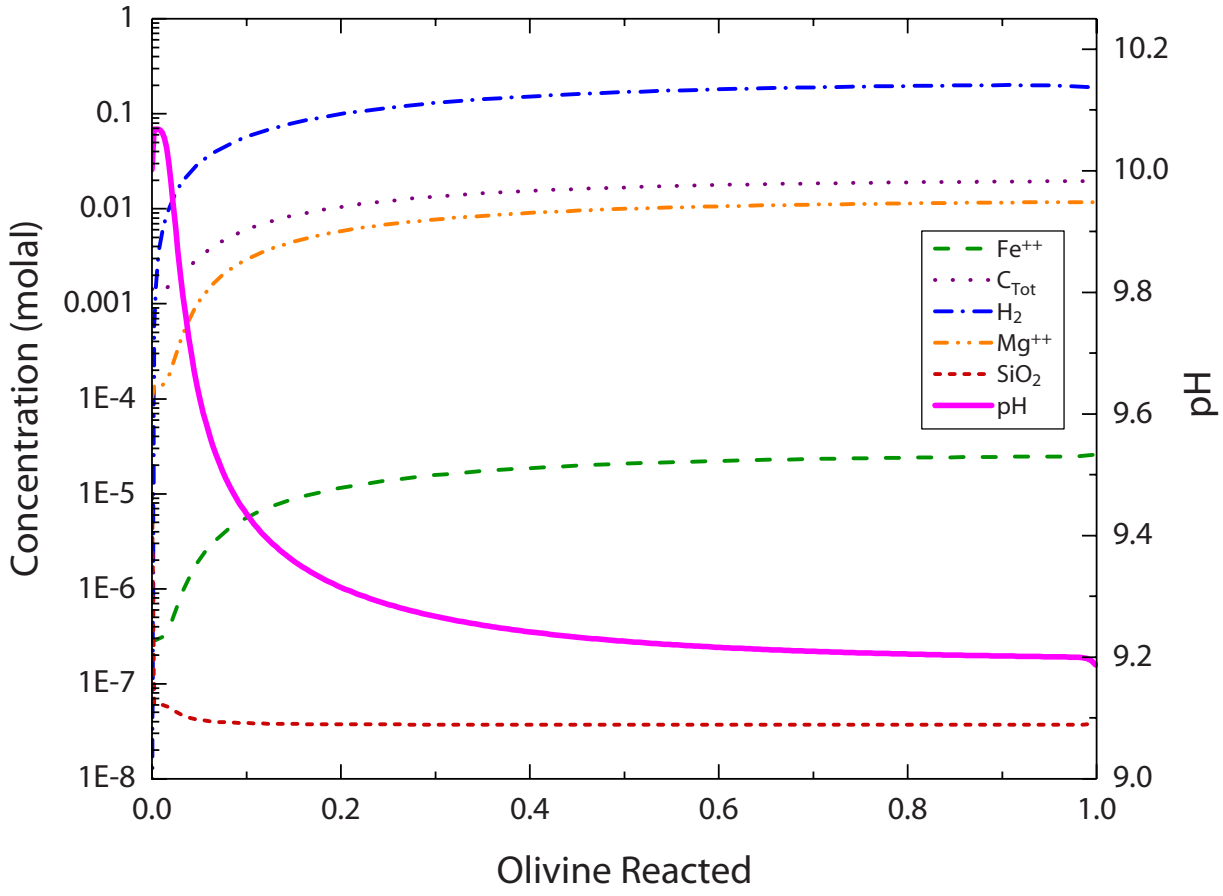

Fig. S11

Concentrations of aqueous components at the midpoint of the simulated domain in coexisting solutions plotted as a function of olivine reaction progress. This simulation corresponds to that from which Figure 3 in the manuscript is produced.

Globally averaged H_2 production on early Mars

Assessing the relative importance of our proposed mechanism for H_2 production is aided by a comparison to estimates of serpentinisation reactions on early Mars. Available evidence in support of serpentinisation on early Mars derives mainly from martian bedrock associated with serpentine minerals (limited to very few isolated regions[20]) and terrestrial analog and modelling studies which attempt to estimate relevant fluxes[17,19]. Although the production rates for H_2 via serpentinisation are poorly constrained, the maximum rates estimated are of the same order of H_2 production via the diagenetic mechanism we propose (at 2% of the early Martian surface participating in surface-subsurface groundwater mixing).

However, it is important to note that serpentine does not necessarily correspond directly to equivalent H_2 production. This is because H_2 production through high temperature serpentinisation is strongly controlled by the partitioning of Fe from rock-forming silicates to Fe^{III}-serpentine or magnetite. In particular, the partitioning of Fe as Fe^{II} severely diminishes the H_2 producing capacity of serpentinisation[123] and recent experimental studies have shown that chemical variables in the serpentinising fluid, such as elevated $SiO_2(aq)$ (as might be expected in subsurface fluids on Mars) severely decrease H_2 production as Fe^{II}-silicates are stabilised in the alteration assemblage[21]. This leads to kinetic effects that limit the effective rate-controlling elementary reaction, brucite silicification[22]. Thus, the role of serpentinisation as a H_2 source on early Mars is unclear, but these factors may have conspired to limit H_2 production far below what most modelling studies assume.

Finally, one factor that may influence globally averaged H_2 production rates relates to the nature of the hydrological regime upon transient or episodic melting (as opposed to widespread warm and wet conditions). If melting and groundwater influx were transient or localised, the chemical dynamics of the diagenetic mechanism would not be influenced. The critical component to H_2 production is the mixing between a subsurface alkaline water body and surface water equilibrated with a relatively high CO_2 atmosphere (**Figure 3** in the manuscript and **Figure S10** and **Figure S11**). Our reactive transport models show that once this mixing takes place, H_2 production is sustained by diffusive transport of Fe^{2+} during olivine dissolution.

However, transient or localised groundwater melting would be expected to impact average global fluxes of H_2 by decreasing the total fraction of the early martian surface across which surface-subsurface mixing takes place. Indeed, more sophisticated global to regional hydrological models that explore a wider range of conditions will refine the dynamics of global H_2 production. It is worth noting, however, that the MSL data returned from Gale Crater support a strong groundwater flux to this location over a significant portion of the timescale recorded by total sediment deposition, which may be on the order of 10^5 to 10^6 years[2,5]. In addition, orbital geomorphic studies document a number of large lake basins fed by groundwater input that may have lasted for similar timescales[41].

References

72. de Leeuw NH, and Cooper TG (2007) Surface simulation studies of the hydration of white rust $Fe(OH)_2$, goethite α-FeO(OH) and hematite α-Fe_2O_3. *Geochimica et Cosmochimica Acta* 71:1655-1673.
73. Blesa MA, and Matijević E (1989) Phase transformations of iron oxides, oxyhydroxides, and hydrous oxides in aqueous media. *Advances in Colloid and Interface Science* 29:173-221.
74. Shipko FJ, and Douglas DL (1956) Stability of ferrous hydroxide precipitates. *The Journal of Physical Chemistry* 60:1519-1523.
75. Regazzoni AE, Urrutia GA, Blesa MA, and Maroto AJG (1981) Some observations on the composition and morphology of synthetic magnetites obtained by different routes. *Journal of Inorganic and Nuclear Chemistry* 43:1489-1493.
76. Olowe AA, Rezel D, and Génin JMR (2006) Mechanism of formation of magnetite from ferrous hydroxide in aqueous corrosion processes. *Hyperfine Interactions* 46:429-436.
77. Baudisch O, and Welo LA (1925) On the Aging of Ferrous Hydroxide and Ferrous Carbonate. *Journal of Biological Chemistry* 64:753-770.
78. Schrauzer GN, and Guth TD (1976) Hydrogen evolving systems. 1. The formation of H_2 from aqueous suspensions of $Fe(OH)_2$ and reactions with reducible substrates, including molecular nitrogen. *Journal of the American Chemical Society* 98:3508-3513.
79. Sugimoto T, and Matijević E (1980) Formation of uniform spherical magnetite particles by crystallization from ferrous hydroxide gels. *Journal of Colloid and Interface Science* 74:227-243.
80. Hansen HCB (2001) Environmental chemistry of iron (II)-iron (III) LDHs (green rusts). *Layered Double Hydroxides: Present and Future. Nova Science Publishers, New York*:413-434.
81. Wander MC, and Schoonen MA (2008) Reduction of N_2 by Fe^{2+} via homogeneous and heterogeneous reactions. Part 1: Evaluation of aqueous photochemical, prebiotic pathways. *Orig Life Evol Biosph* 38:127-37.
82. Wander MC, Rosso KM, and Schoonen MA (2007) Structure and charge hopping dynamics in green rust. *The Journal of Physical Chemistry C* 111:11414-11423.
83. Génin J-MR, Ruby C, Géhin A, and Refait P (2006) Synthesis of green rusts by oxidation of $Fe(OH)_2$, their products of oxidation and reduction of ferric oxyhydroxides;–pH Pourbaix diagrams. *Comptes Rendus Geoscience* 338:433-446.
84. Drissi H, Refait P, and Génin J-M (1994) The oxidation of $Fe(OH)_2$ in the presence of carbonate ions: structure of carbonate green rust one. *Hyperfine Interactions* 90:395-400.
85. Refait P, Abdelmoula M, and Génin J-M (1998) Mechanisms of formation and structure of green rust one in aqueous corrosion of iron in the presence of chloride ions. *Corrosion Science* 40:1547-1560.
86. Evans UR, and Wanklyn JN (1948) Evolution of hydrogen from ferrous hydroxide. *Nature* 162:27-28.
87. Yamane I, and Sato K (1968) Initial rapid drop of oxidation-reduction potential in submerged air-dried soils. *Soil Science and Plant Nutrition* 14:68-72.
88. Morrill PL, Kuenen JG, Johnson OJ, Suzuki S, Rietze A, Sessions AL, Fogel ML, and Nealson KH (2013) Geochemistry and geobiology of a present-day serpentinization site in California: The Cedars. *Geochimica et Cosmochimica Acta* 109:222-240.

89. Stumm W, and Morgan JJ (1996) *Aquatic Chemistry: An Introduction Emphasizing Chemical Equilibria in Natural Waters* (John Wiley & Sons, New York).
90. Sigg L (2000) in *Redox* (Springer), p 1-12.
91. Refait P, Bon C, Simon L, Bourrié G, Trolard F, Bessiere J, and Génin J-M (1999) Chemical composition and Gibbs standard free energy of formation of Fe(II)-Fe (III) hydroxysulphate green rust and Fe(II) hydroxide. *Clay Minerals* 34:499-510.
92. Drissi SH, Refait P, Abdelmoula M, and Génin JMR (1995) The preparation and thermodynamic properties of Fe(II)-Fe(III) hydroxide-carbonate (green rust I); Pourbaix diagram of iron in carbonate-containing aqueous media. *Corrosion science* 37:2025-2041.
93. Ruby C, Gehin A, Aissa R, Ghanbaja J, Abdelmoula M, and Genin JMR (2006) Chemical stability of hydroxysulphate green rust synthesized in the presence of foreign anions: carbonate, phosphate and silicate. *Hyperfine Interactions*167:803-807.
94. Guilbaud R, White ML, and Poulton SW (2013) Surface charge and growth of sulphate and carbonate green rust in aqueous media. *Geochimica et Cosmochimica Acta* 108:141-153.
95. Sumoondur A, Shaw S, Ahmed I, and Benning LG (2008) Green rust as a precursor for magnetite: an in-situ synchrotron based study. *Mineralogical Magazine* 72:201-204.
96. Murad E, and Schwertmann U (1993) Temporal stability of a fine-grained magnetite. *Clays and Clay Minerals* 41:111-113.
97. Tang J, Myers M, Bosnick KA, and Brus LE (2003) Magnetite Fe_3O_4 Nanocrystals: Spectroscopic Observation of Aqueous Oxidation Kinetics. *J Phys Chem B* 107:7501-7506.
98. Radha AV, and Navrotsky A (2013) Thermodynamics of Carbonates. *Reviews in Mineralogy and Geochemistry* 77:73-121.
99. Bruno J, Wersin P, and Stumm W (1992) On the influence of carbonate in mineral dissolution: II. The solubility of $FeCO_3$(s) at 25°C and 1 atm total pressure. *Geochimica et Cosmochimica Acta* 56:1149 - 1155.
100. Wersin P, Charlet L, Karthein R, and Stumm W (1989) From adsorption to precipitation: sorption of Mn^{2+} on $FeCO_3$(s). *Geochimica et Cosmochimica Acta* 53:2787-2796.
101. Carothers WW, Adami LH, and Rosenbauer RJ (1988) Experimental oxygen isotope fractionation between siderite-water and phosphoric acid liberated CO_2-siderite. *Geochimica et Cosmochimica Acta* 52:2445-2450.
102. Romanek CS, Jiménez-López C, Navarro AR, Sánchez-Román M, Sahai N, and Coleman M (2009) Inorganic synthesis of Fe-Ca-Mg carbonates at low temperature. *Geochimica et Cosmochimica Acta* 73:5361-5376.
103. Wiesli RA, Beard BL, and Johnson CM (2004) Experimental determination of Fe isotope fractionation between aqueous Fe(II), siderite and "green rust" in abiotic systems. *Chemical geology* 211:343-362.
104. Johnson ML (1991) *Ferrous Carbonate Precipitation Kinetics - A Temperature Ramped Approach* (Ph. D. Thesis, Rice University, Houston, Texas).
105. Jimenez-Lopez C, and Romanek CS (2004) Precipitation kinetics and carbon isotope partitioning of inorganic siderite at 25° C and 1 atm. *Geochimica et Cosmochimica Acta* 68:557-571.
106. Siebach KL, Grotzinger JP, Kah LC, Stack KM, Malin M, Léveillé R, and Sumner DY (2014) Subaqueous Shrinkage Cracks in the Sheepbed Mudstone: Implications for Early

Fluid Diagenesis, Gale Crater, Mars. *Journal of Geophysical Research: Planets* 119:1597-1613.
107. Hurowitz JA, Fischer WW, Tosca NJ, and Milliken RE (2010) Origin of acidic surface waters and the evolution of atmospheric chemistry on early Mars. *Nature Geoscience* 3:323-326.
108. Schieber J, Bish D, Coleman M, Reed M, Hausrath EM, Cosgrove J, Gupta S, Minitti ME, Edgett KS, and Malin M (2016) Encounters with an unearthly mudstone: Understanding the first mudstone found on Mars. *Sedimentology* 64:311-358.
109. Nagy KL (1995) in *Chemical Weathering Rates of Silicate Minerals*, editor White AF, Brantley SL, and Ribbe PH (Mineralogical Society of America, Washington, D.C.).
110. Tardy Y, and Fritz B (1981) An ideal solid solution model for calculating solubility of clay minerals. *Clay minerals* 16:361-373.
111. Crowe SA, Maresca JA, Jones C, Sturm A, Henny C, Fowle DA, Cox RP, Delong EF, and Canfield DE (2014) Deep-water anoxygenic photosythesis in a ferruginous chemocline. *Geobiology* 12:322-39.
112. Velde B, and Meunier A (2008) *The Origin of Clay Minerals in Soils and Weathered Rocks* (Springer-Verlag, Berlin).
113. Barnes I, O'Neil JR, and Trescases J-J (1978) Present day serpentinization in New Caledonia, Oman and Yugoslavia. *Geochimica et Cosmochimica Acta* 42:144-145.
114. Neal C, and Stanger G (1983) Hydrogen generation from mantle source rocks in Oman. *Earth and Planetary Science Letters* 66:315-320.
115. Monnin C, Chavagnac V, Boulart C, Ménez B, et al. (2014) Fluid chemistry of the low temperature hyperalkaline hydrothermal system of Prony Bay (New Caledonia). *Biogeosciences* 11:5687-5706
116. Pokrovsky OS, and Schott J (2000) Forsterite surface composition in aqueous solutions: A combined potentiometric, electrokinetic, and spectroscopic approach. *Geochimica et Cosmochimica Acta* 64:3299-3312.
117. Lichtner PC, et al. (2017) PFLOTRAN Web page.
118. Potter P, and Maynard JB (2005) *Mud and Mudstones, Introduction and Overview* (Springer, New York).
119. Oelkers EH, Helgeson HC (1988) Calculation of the thermodynamic and transport properties of aqueous species at high pressures and temperatures: Aqueous tracer diffusion coefficients of ions to 1000^{o}C and 5 kb. *Geochim Cosmochim Acta* 52:63–85.
120. Tosca NJ, Macdonald FA, Strauss J V., Johnston DT, Knoll AH (2011) Sedimentary talc in Neoproterozoic carbonate successions. *Earth Planet Sci Lett* 306(1–2):11–22.
121. White AF, Brantley SL (2003) The effect of time on the weathering of silicate minerals: Why do weathering rates differ in the laboratory and field? *Chem Geol* 202:479–506.
122. Neubeck A, Duc NT, Bastviken D, Crill P, Holm NG (2011) Formation of H_2 and CH_4 by weathering of olivine at temperatures between 30 and 70°C. *Geochem Trans* 12(1):6.
123. McCollom TM, and Bach W (2009) Thermodynamic constraints on hydrogen generation during serpentinization of ultramafic rocks. *Geochimica et Cosmochimica Acta*, 73: 856-875.